The Astrophysical Journal, 960:91 (13pp), 2024 January 1 https://doi.org/10.3847/1538-4357/acf9f3

How Solar Soft X-Ray Irradiance Is Affected by the Size of Field of View

Aki Takeda[1] and Shannon Boland[2]
[1] Department of Physics, Montana State University Bozeman, MT 59717, USA
[2] University of Wyoming, 1000 E. University Avenue, Laramie, WY 82071, USA
Received 2023 May 7; revised 2023 July 30; accepted 2023 September 13; published 2023 December 29

Abstract

Soft X-ray images of the Sun obtained with multiple broadband filters provide a simple and useful method to calculate averaged coronal temperature and emission measure, from which we can further calculate solar X-ray irradiance in physical units, e.g., watts per square meter. However, X-ray telescopes are often designed for pursuing high spatial resolution, and thus the field of view (FOV) of full-Sun images is often limited over the limb, extending to only $\sim$1.3 $R_\odot$. This indicates that the irradiance obtained from the limited FOV may underestimate the true full-Sun irradiance by failing to count the contribution from outside the FOV. This work uses Hinode/X-Ray Telescope (XRT) coronal images observed up to 1.7 $R_\odot$ to investigate the fraction of irradiance excluded from the FOVs limited in size. The analysis indicates that the irradiance obtained within 1.1 $R_\odot$, which is used for XRT irradiance study, excludes $\sim$3.5%/$\sim$7% of irradiance relative to the value within 1.2/1.7 $R_\odot$, respectively, for the active corona observed in 2022 July. In contrast, the excluded fraction increases to $\sim$7%/$\sim$13%, respectively, for the minimum corona observed in 2009 August. To further investigate the dependence of exclusion fraction on the Sun's activity level, we process mission long Yohkoh/Soft X-ray Telescope full-Sun images to compare the irradiance within 1.1 and 0.9 $R_\odot$ with that obtained from the maximum FOV of 1.2 $R_\odot$. We confirm that the exclusion fraction is the largest in the period around solar minimum. We also find that the average value of exclusion fraction is slightly but measurably larger in the rising phase than the declining phase of the solar cycle.

Unified Astronomy Thesaurus concepts: Solar corona (1483); Solar cycle (1487)

1. Introduction

The X-ray radiation from the Sun is a well-accepted indicator of the Sun's release of magnetic energy, while its long-term variation provides the valuable records of the Sun's evolution as a star. Above the Earth, solar X-rays ionize the atmospheric particles and increases electron density of the ionosphere, whose abrupt disturbance can deteriorate radio communication and navigation accuracy or endanger the orbital and mechanical stability of low Earth orbit satellites. Whereas hard X-ray emission (having wavelength shorter than 0.1 nm) from the Sun is effectively detected on the occasion of energetic events like flares, soft X-ray (wavelength range roughly 0.1–10 nm) includes the emission produced by the steady component of the solar corona with the temperature range of 1–2 MK and thus suitable for long-term continuous monitoring of our Sun's activity level.

The X-Ray Sensor (XRS) on board a series of Geostationary Operational Environmental Satellites (GOES) has decades of history (since 1970s) of solar soft X-ray flux observations in the short (0.05–0.4 nm) and long (0.1–0.8 nm) wavelength bands (Garcia 1994; White et al. 2005). While the XRS had been traditionally utilizing ionization chambers (until GOES-15), the recent series equips photodiodes as detectors (Chamberlin et al. 2009).

The Solar EUV Experiment (SEE; Woods et al. 2005) is one of the instruments aboard the Thermosphere Ionosphere Mesosphere Energetics and Dynamics mission. SEE has been providing the solar spectral irradiance in the vacuum ultraviolet wavelength range (0–200 nm) since January 2002. The soft X-ray portion of irradiance is obtained with silicon photodiodes that form the XUV Photometer System measuring the wavelength range of 0.1–27 nm. The improved versions of the detectors of this type are employed in recent missions like the Miniature X-ray Solar Spectrometer (MinXSS) CubeSat series since 2016 (Moore et al. 2018) and the Solar X-ray Monitor on board the Chandrayaan-2 mission since 2019 September (Mithun et al. 2020).

The Extreme Ultraviolet Variability Experiment (Woods et al. 2012) on board the Solar Dynamics Observatory has two instruments capable of measuring solar soft X-ray irradiance. The Extreme Ultraviolet Spectrophotometer (Didkovsky et al. 2012) utilizes the diffraction transmission grating and photodiode detectors. The soft X-ray component from 0.1 to 7.0 nm is measured as the zeroth-order band from the grating since 2010 May. The Solar Aspect Monitor (SAM; Woods et al. 2012, Section 3.3) is a pinhole camera with a metallic filter that projects the full-Sun soft X-ray image onto the CCD. Lin et al. (2016) proposed the technique for isolating the solar irradiance from the contamination included in the SAM signal and derived soft X-ray irradiance integrated over 0.01–7 nm wavelength since 2010 May. In 2014 May, however, the SAM was turned off due to a CCD power supply failure.

The Soft X-ray Telescope (SXT; Tsuneta et al. 1991) is a grazing incidence telescope on board the Yohkoh satellite, which was in operation for the period 1991 September through 2001 December. Using SXT full-Sun images pairs obtained with two broadband filters, Takeda et al. (2019) calculated the averaged temperature, emission measure (EM) of the corona, and soft X-ray irradiance (0.3–3 nm) for the whole mission period.

The X-Ray Telescope (XRT; Golub et al. 2007) on board the Hinode satellite is the successor to Yohkoh/SXT, designed for the coronal imaging with better spatial resolution and broader

temperature coverage. Using the XRT full-Sun level-2 science composite images (Takeda et al. 2016), the soft X-ray irradiance study similar to that with SXT images is underway (A. Takeda, 2024 in preparation). While SXT irradiance was derived from the coronal signal collected within 1.2 $R_\odot$, XRT collects signals within 1.1 $R_\odot$ due to its smaller full FOV than SXT. This indicates that the XRT irradiance is somewhat underestimated compared with the cases the signals were collected from wider area: when the Sun's activity level is high, the bright structures often extend over the range of signal collection for irradiance study (e.g., 1.1 $R_\odot$ for XRT) and not counted in the calculation of irradiance. On the other hand, when the Sun is in minimum condition, the off-limb corona is also minimal and featureless, but the small difference in off-limb signals has a larger contribution to the total brightness of the corona because the disk corona is the darkest.

The purpose of this work is to investigate quantitatively how the limited FOV of the instrument affects the calculation of full-Sun irradiance. The emphasis is on providing basic data to relatively correct the a series of irradiance values obtained with different sizes of FOV (e.g., Yohkoh/SXT and Hinode/XRT) rather than increasing the precision of the measurement of the X-ray irradiance on a particular day. Using imagery, we can derive X-ray irradiance from different distances from the Sun center according to instrumental limitation, but there is no previous study that discusses the effect of the size of signal collection on the derived X-ray irradiance. We analyze the Hinode/XRT full FOV images obtained in active phase of the Sun in 2022 and in the minimum phase in 2009 to calculate irradiance from the signals collected from different size of FOV. We also reprocess the Yohkoh/SXT irradiance data used in Takeda et al. (2019) to measure the difference of the irradiances obtained from different sizes of FOV and its variation over the solar cycle.

2. Hinode/XRT Data Preparation

The XRT full-Sun images obtained in the synoptic programs are usually taken with two or three different exposure times (short-long or short-medium-long) for each selected X-ray analysis filter. They are processed into a single composite image to avoid saturation of bright structures and keep high signal-to-noise ratio (S/N) of dark regions (Takeda et al. 2016). Photometric analysis of high-altitude corona like this work requires an even higher level of S/N. Therefore, special observation was performed in 2022 July to study the high-altitude corona of the active Sun up to 1.7 $R_\odot$. The coronal images at solar minimum was prepared by reprocessing the archived full-Sun synoptic composite images obtained in 2009 August to study off-limb corona up to 1.3 $R_\odot$.

2.1. Active Corona Image Preparation

The high-altitude corona above the northeast (NE) limb was observed on 2022 July 16, using multiple filters and exposure times listed in Table 1. The GOES16/XRS soft X-ray flux (1–8 Å band) was around C2 level (2×10^{-6} W m^{-2}) at the time of observation. Hereafter we refer to the 2022 July 16 corona as "active corona."

The spectral and temperature responses of the XRT analysis filters are found in Narukage et al. (2011). Roughly speaking, the Al-mesh, Al-poly, and thin-Be filters effectively detect from cooler to hotter coronal plasma in this order. Each image has the size of 1024 x 1024 pixels with the spatial resolution of $2\farcs06$ pix^{-1}. The XRT pointing during the observation was located at ($-555\farcs8$, $551\farcs3$) in heliocentric coordinates, by which the XRT full FOV can cover the NE quadrant of the Sun up to 1.7 $R_\odot$ (see Figure 1).

In this observation, two sets of composite images were obtained for each filter. While regular synoptic programs take a single long exposure for each filter, this observation uses multiple long exposures to achieve better S/N at the high-altitude region. Those multiple long exposures were summed up to a single long exposure image then used in the usual procedure to create composite images (see Takeda et al. 2016 for details). The two composite images processed for each filter were finally added and normalized with respect to the exposure time.

XRT images after 2012 May 9 suffer from visible stray light contamination caused by the repeated generation of a small crack on the XRT prefilter. As of 2022 July, the stray light component included in the Al-mesh and Al-poly filter needs to be corrected, while the one included in the thin-Be images is still negligible. We therefore performed the stray light measurement on 2022 July 19, with the Al-mesh and Al-poly filters at the same pointing as that of the high corona observation. The obtained stray light images were normalized with respect to the exposure times and subtracted from the corresponding Al-mesh and Al-poly composite images of the high corona.

Figure 1 shows the coronal images above the NE limb prepared as described above for three X-ray filters of XRT. The small horizontal intensity enhancement that appeared about 1.5 to 1.7 $R_\odot$ in Al-mesh and Al-poly images is a ghost pattern of XRT, which probably is a scattered light component specific to the telescope pointing. We are unable to remove it with the standard procedure for scattered light correction, but it turned out to have a negligible effect on our analysis (see averaged radial plot in Figure 13).

2.2. Minimum Corona Image Preparation

The images of the corona on 2009 August 12 displayed in Figure 2 were prepared by using two archived composite images obtained closely in time. The two composite images were added to improve S/N and normalized with respect to their exposure time. Note that these images obtained before the XRT prefilter failure are free from stray light contamination. Table 2 shows the list of original images used to create each composite image.

The observed corona has no active region on the solar disk or limb, showing typical corona of the solar minimum. The GOES10/XRS flux was below its detection level at around 3×10^{-9} W m^{-2}. We hereafter term the 2009 August 12 corona "minimum corona."

3. Data Analysis

3.1. Collection of Coronal Signals

Coronal signals (measured in the unit of data numbers in this work) are collected by applying several different sizes of masking image tailored for the active and minimum periods of the Sun, respectively.

The active Sun signals from the NE quadrant were measured by masking the area outside a quarter sector of the disk whose center coincides with the Sun center coordinates (see Figure 3,

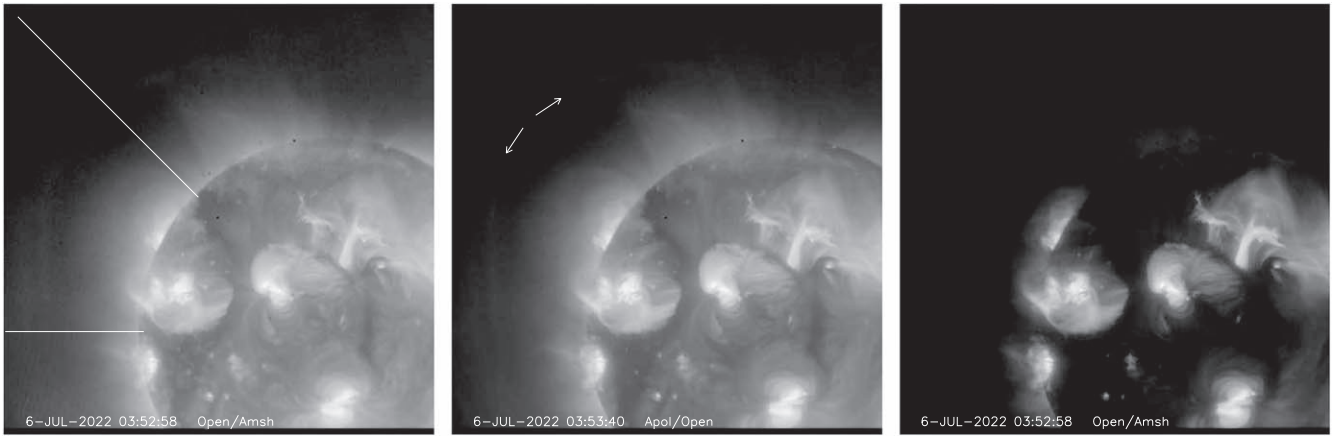

Figure 1. XRT composite images of the active corona processed from the images listed in Table 1. Left: image processed for the Al-mesh filter. Two lines are the location of the intensity profile shown in Figure 13. Middle: for the Al-poly filter. Two arrows indicate the location of ghost pattern of XRT. Right: for the thin-Be filter.

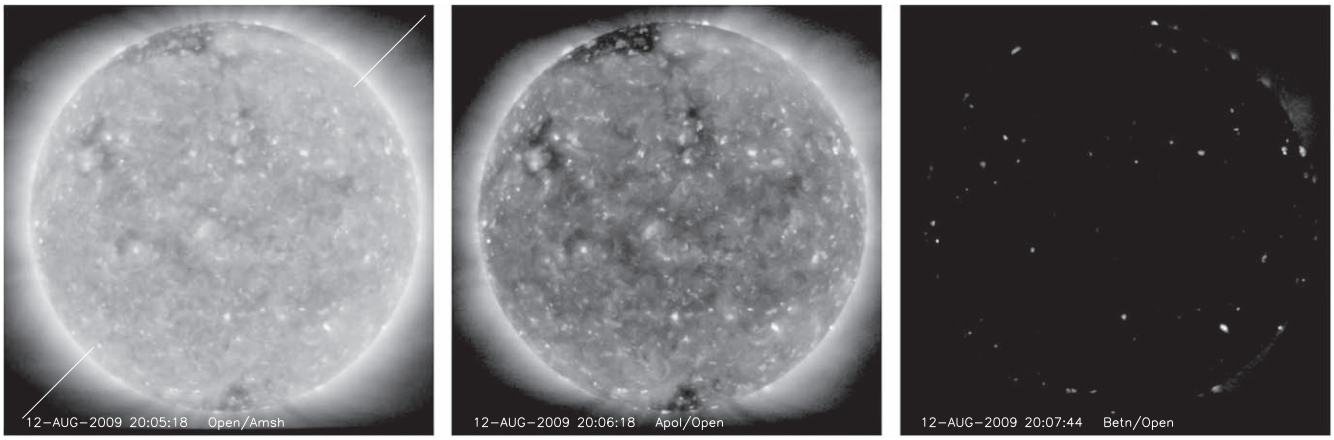

Figure 2. XRT composite images of the minimum corona processed from the images listed in Table 2. Left: image processed for the Al-mesh filter. Middle: for the Al-poly filter. Right: for the thin-Be filter. Two lines in the Al-mesh image show the location of the intensity profile shown in Figure 14.

Table 1
XRT Images Used for the Study of the Active Corona

Date	Al-mesh Time	Exposure Time (s)	Date	Al-poly Time	Exposure Time (s)	Date	Thin-Be Time	Exposure Time (s)
(1)	(2)	(3)	(4)	(5)	(6)	(7)	(8)	(9)
16 Jul 2022	03:48:29	0.0020	16 Jul 2022	03:49:19	0.0123	16 Jul 2022	03:50:01	0.0163
16 Jul 2022	03:48:41	0.1280	16 Jul 2022	03:49:25	0.1812	16 Jul 2022	03:50:06	0.5127
16 Jul 2022	03:48:47	0.7255	16 Jul 2022	03:49:31	1.4454	16 Jul 2022	03:50:18	2.8977
16 Jul 2022	03:48:53	0.7251	16 Jul 2022	03:49:39	1.4438	16 Jul 2022	03:50:26	2.8995
16 Jul 2022	03:48:59	0.7255	16 Jul 2022	03:49:46	1.4453	16 Jul 2022	03:50:34	2.8989
16 Jul 2022	03:49:11	0.7240	16 Jul 2022	03:49:52	1.4449	16 Jul 2022	03:50:48	2.8977
16 Jul 2022	03:52:22	0.0020	16 Jul 2022	03:53:06	0.0123	16 Jul 2022	03:50:56	2.8992
16 Jul 2022	03:52:28	0.1280	16 Jul 2022	03:53:12	0.1812	16 Jul 2022	03:51:04	2.8989
16 Jul 2022	03:52:33	0.7255	16 Jul 2022	03:53:20	1.4438	16 Jul 2022	03:53:48	0.0163
16 Jul 2022	03:52:39	0.7250	16 Jul 2022	03:53:27	1.4453	16 Jul 2022	03:54:00	0.5120
16 Jul 2022	03:52:52	0.7239	16 Jul 2022	03:53:33	1.4449	16 Jul 2022	03:54:06	2.8992
16 Jul 2022	03:52:58	0.7255	16 Jul 2022	03:53:40	1.4453	16 Jul 2022	03:54:14	2.8989
...	...	...	...	...	...	16 Jul 2022	03:54:22	2.8992
...	...	...	...	...	...	16 Jul 2022	03:54:36	2.8977
...	...	...	...	...	...	16 Jul 2022	03:54:47	2.8992
19 Jul 2022	19:09:02	(*)	19 Jul 2022	19:09:11	(*)	16 Jul 2022	03:55:07	2.8977

Note. See the text in Section 2.1 for details. The asterisk indicates stray light images.

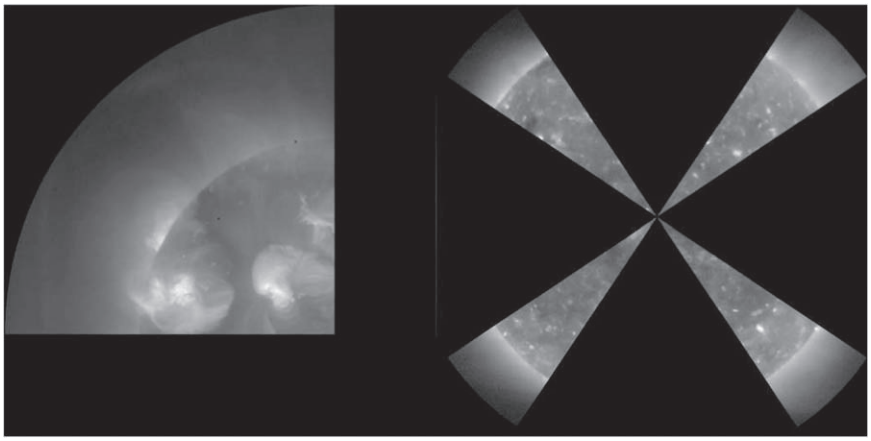

Figure 3. Masking images used for the analysis of active corona (left) and minimum corona (right).

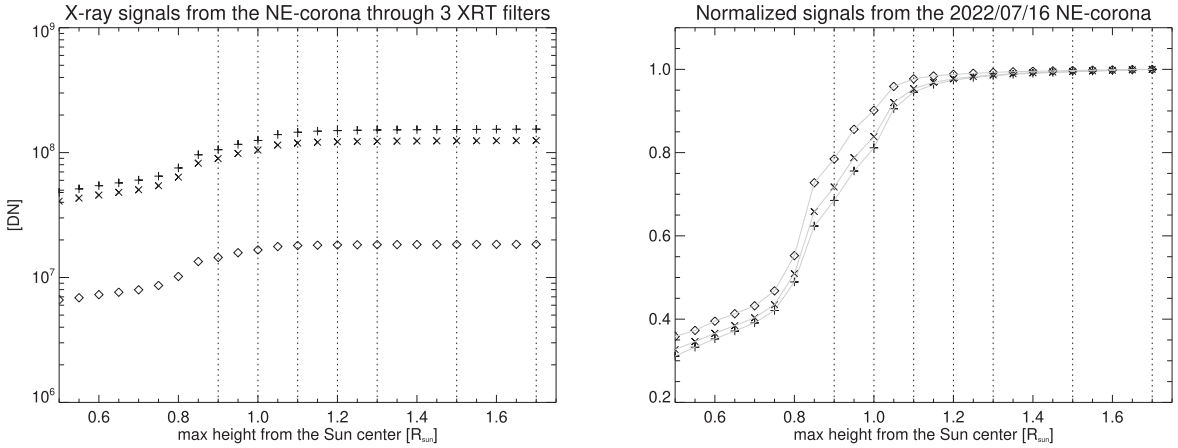

Figure 4. Left: total XRT signals from the NE region of the 2022 July 16 corona included in the different sizes of open area of the masking image shown in the Figure 3. The plus/cross/diamond symbols indicate the observed signals with XRT's Al-mesh/Al-poly/thin-Be analysis filters, respectively. Right: same as the left plot, but signals are normalized with respect to the value at 1.7 $R_\odot$ for each filter. The vertical dotted lines indicate the positions where the data number and its normalized value are listed in Table 3.

Table 2
XRT Images Used for the Study of the Minimum Corona

	Al-mesh			Al-poly			Thin-Be	
Date	Time	Exposure Time (s)	Date	Time	Exposure Time (s)	Date	Time	Exposure Time (s)
(1)	(2)	(3)	(4)	(5)	(6)	(7)	(8)	(9)
12 Aug 2009	20:05:12	0.5121	12 Aug 2009	20:06:13	0.5128	12 Aug 2009	20:07:44	32.7680
12 Aug 2009	20:05:18	5.7971	12 Aug 2009	20:06:18	5.7971	12 Aug 2009	20:16:44	32.7680
12 Aug 2009	20:14:12	0.5121	12 Aug 2009	20:15:13	0.5128	...	...	...
12 Aug 2009	20:14:18	5.7971	12 Aug 2009	20:15:18	5.7971	...	...	...

left image). By changing the radius of the sector area from 0.5 to 1.7 $R_\odot$ in steps of 0.1 $R_\odot$, we can collect the total signal from the NE quarter of the corona included in the corresponding size of the open area. Figure 4 shows the variation of XRT signals of the active corona, collected from the FOVs of varying size shown in Figure 3. Table 3 shows the readings of the data in Figure 4 for the selected sizes of FOV.

In order to study the high-altitude region of the minimum corona, we applied the quadplex masking image (see Figure 3, right image), each of whose parts is made of a sector with the central angle of 22.5° and the radius varying from 0.5 to the maximum of 1.3 $R_\odot$. By adding the signals collected from the four areas, we can virtually obtain the signals from a quarter area relative to the whole Sun.

Figure 5 shows the variation of XRT signals of the minimum corona, collected from different sizes of FOV. Note that we use the term FOV to indicate the open area of the masking image of this unusual shape. We then extend the curve of integrated signals up to 1.7 $R_\odot$ using the estimated radial attenuation rate of the signals of each filter. Details are described in Appendix A. The extended signal curves and their normalized

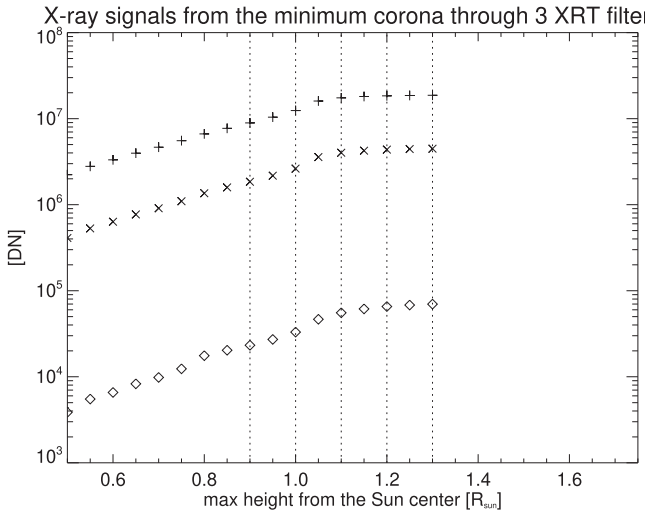

Figure 5. Total XRT signals of the minimum corona included in the different sizes of open area of the masking image shown in Figure 3. The plus cross/diamond/square symbols indicate the observed signals with XRT's Al-mesh/Al-poly/thin-Be analysis filters, respectively.

Table 3
XRT Signals of the Active Corona Observed with Three X-Ray Filters

FOV height ($R_\odot$)	Al-mesh		Al-poly		Thin-Be	
	(10^8 DN)	Rel.	(10^8 DN)	Rel.	(10^8 DN)	Rel.
0.9	1.06	0.685	0.896	0.717	0.145	0.785
1.0	1.25	0.812	1.05	0.838	0.166	0.901
1.1	1.46	0.945	1.19	0.954	0.180	0.977
1.2	1.50	0.974	1.22	0.977	0.182	0.988
1.3	1.52	0.985	1.23	0.987	0.183	0.993
1.5	1.53	0.994	1.24	0.995	0.184	0.997
1.7	1.54	1.00	1.25	1.00	0.185	1.00

Note. Readings of the plot in Figure 4 for selected heights of the FOV. Signals are in the unit of 10^8 DN. Normalization was made relative to the value at 1.7 $R_\odot$ for each filter.

values are plotted in Figure 6. Table 4 shows the readings of the data in Figure 6 for five selected heights of FOV.

3.2. Derivation of Averaged Temperatures and Emission Measures

Pairs of derived XRT signals obtained for two different filters are used to calculate the FOV-averaged electron temperature (Te) and EM through the filter ratio method (see Narukage et al. 2011 for its application to XRT data). The temperature response function of each filter was recalculated using the latest atomic data by CHIANTI version 10.0.2 (Dere et al. 1997; Del Zanna et al. 2021) and the latest correction of XRT effective area functions. The XRT temperature response functions vary with time due to the aging of the instrument, i.e., increasing visible stray light component included in the X-ray signals and growing contaminant layer on CCD and X-ray filters, which both modify XRT effective area functions. We selected two filter ratios, Al-poly/Al-mesh and thin-Be/Al-poly to calculate Te and EM. The filter ratio curves used in this analysis are demonstrated in Figure 7.

Table 4
XRT Signals of the Minimum Corona Observed with Three X-Ray Filters

FOV height ($R_\odot$)	Al-mesh		Al-poly		Thin-Be	
	(10^6 DN)	Rel.	(10^6 DN)	Rel.	(10^6 DN)	Rel.
0.9	8.94	0.469	1.85	0.399	0.0234	0.303
1.0	12.4	0.652	2.63	0.567	0.0330	0.427
1.1	17.5	0.916	4.02	0.868	0.0553	0.715
1.2	18.4	0.965	4.36	0.943	0.0655	0.847
1.3	18.7	0.980	4.48	0.967	0.0698	0.903
1.5	18.9	0.991	4.55	0.984	0.0735	0.951
1.7	19.1	1.00	4.63	1.00	0.0773	1.00

Note. Readings of the plot in Figure 6 for selected heights of the FOV. Signals are in the unit of 10^6 DN. Normalization was made relative to the value at 1.7 $R_\odot$ for each filter.

The Te and EM averaged over the FOVs with different heights for the active corona were plotted in Figure 8. The plots in Figure 9 are the corresponding Te and EM for the minimum corona.

Compared with the Al-poly/Al-mesh filter pair, the thin-Be/Al-poly pair generally yields higher Te and lower EM. This result is consistent with the difference of the temperature response of three filters: Al-mesh, Al-poly, and thin-Be filters have larger to smaller response to the cooler plasma around 1 MK in this order. As a general caveat to the filter ratio analysis, these two sets of Te and EM do not mean that they exist together as hot and cool components in the observed corona. Note that each set is derived as the result of isothermal assumption.

3.3. Calculation of Soft X-Ray Irradiance

From the derived Te and EM, the isothermal coronal spectrum is calculated using the CHIANTI atomic DB ver. 10.0 in accordance with the recalculated XRT response functions, i.e., the assumption of traditional coronal elemental abundance (`Sun_coronal_1992_feldman_ext.abund`) and standard ionization equilibrium data (`chianti.ioneq`). The soft X-ray irradiance in the unit of watts per squared meter is finally obtained by integrating the spectral energy for the wavelength range of 0.5–6 nm. This spectral range was chosen considering the fact that the XRT effective area with thin X-ray analysis filters (e.g., Al-mesh and Al-poly) roughly has 10^{-2} of the peak value. However, it is also possible to calculate the irradiance for a different spectral range to compare with the results from other instruments, like GOES/XRS, Yohkoh/SXT, MinXSS/X123, etc.

4. Results

The XRT irradiance from a quarter area of the Sun was measured up to 1.7 $R_\odot$ for the active and the minimum phases of the solar cycle through the method described in Section 3. The irradiance obtained from the two filter pairs are plotted in Figure 10. Those irradiance values and their normalized values relative to those at 1.7 $R_\odot$ are listed in Tables 5 and 6 for selected heights of FOV.

Regarding the active corona, the observed curves of irradiance from both filter pairs are well saturated at the region higher than 1.5 $R_\odot$. We therefore assume for each filter pair that

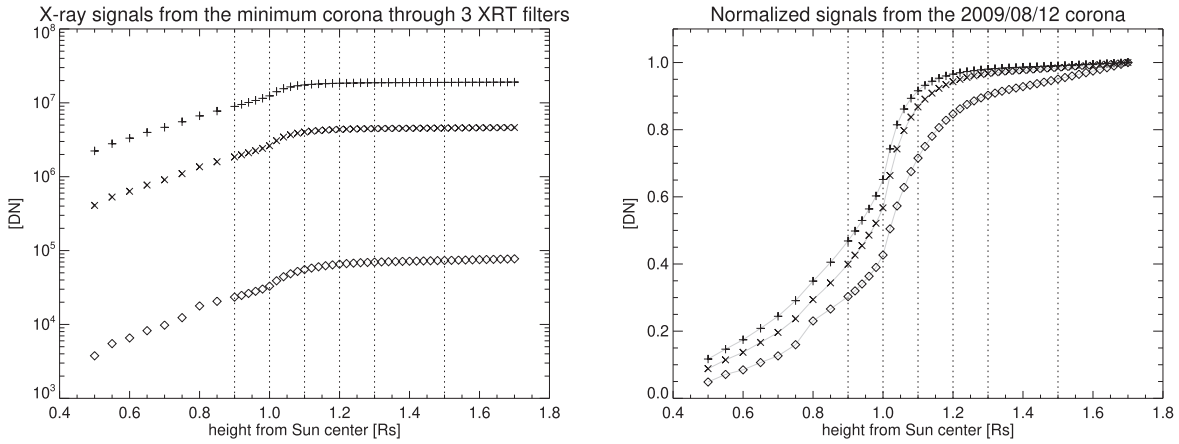

Figure 6. Left: total XRT signals of the minimum corona extended to the height 1.7 $R_\odot$. See the text in Section 3.1 for details. Right: same as the left plot, but signals are normalized with respect to the value at 1.7 $R_\odot$ for each filter. The vertical dotted lines indicate the positions where the data number and its normalized value are listed in Table 4.

the irradiance with the FOV height of 1.7 $R_\odot$ represents the value from the whole Sun (to be exact, a quarter of it, due to the shape of the FOV). Compared with this full-Sun irradiance, the XRT irradiance, whose signal is collected within 1.1 $R_\odot$, turned out to measure 6%–7% less by rough estimate. If we could collect signals within 1.2 $R_\odot$ like Yohkoh/SXT as in Takeda et al. (2019), then shortage will be reduced to 3%–4%. In order to measure the irradiance with the shortage less than 1%, it is desirable to use the FOV with 1.5 $R_\odot$.

Regarding the minimum corona, we will also assume that the irradiance within 1.7 $R_\odot$ represents the full-Sun value. However, the observation of the minimum corona with the thicker filter is unreliable due to low signal level, and thus, the irradiance from the thin-Be/Al-poly filter pair is unreliable relative to the result from the Al-poly/Al-mesh filter pair. Therefore, our analysis indicates that the XRT irradiance (within 1.1 $R_\odot$) for the minimum corona fails to measure roughly 13% of the full-Sun irradiance, which is a larger rate than the case of active corona. When we widen the FOV to 1.2 $R_\odot$, the shortage is reduced to 6%, which is still larger than the active Sun case. At the FOV size of 1.5 $R_\odot$, the exclusion fraction becomes less than 1%, the same level as the active Sun case. Obviously, these values of exclusion fraction depend on the height we regard as equivalent to the full-Sun irradiance (1.7 $R_\odot$ was assumed here). As a trial, we recalculated the exclusion fraction relative to 1.5 $R_\odot$ FOV, at which height we can barely detect the coronal signals at the corner of images in Figure 2. The results turn out to be 13% and 5% at 1.1 $R_\odot$ and 1.2 $R_\odot$, respectively, which are still significantly larger than the active Sun case.

For the active corona, the exclusion fractions of the irradiance tend to be larger than those of signals for the same size of FOV: for the FOV size of 1.1 $R_\odot$, the signal exclusion fraction of the Al-mesh, Al-poly, and thin-Be filters are calculated from Table 4 as 5.5%, 4.6%,and 2.2%, respectively. From Table 6, on the other hand, the exclusion fractions of irradiance are 6.3% from Al-poly/Al-mesh filter ratio and 7.1% from thin-Be/Al-poly. Those differences decrease with height. For the minimum corona, however, we do not clearly see this trend, probably because of the uncertainty of the expansion of the minimum corona and also uncertainty of the measurements using the thicker filter.

This work uses summed XRT signals collected from a wide expanse of area comparable to a quarter of the solar disk. Therefore, the statistical uncertainties (or often referred to as photon-counting error) are kept very small. Nonstatistical uncertainties included in XRT signals are discussed in detail in Kobelski et al. (2014). Those nonstatistical errors such as signal loss due to JPEG compression, uncertainties of vignette and dark corrections, etc., turned out also to be kept small for our summed signals. Table 7 demonstrates the uncertainties included in the XRT signals collected from the different size of FOVs for active and minimum corona. Statistical uncertainties were calculated from the obtained filter ratio temperature utilizing the XRT analysis software, `xrt_cvfact.pro` (Narukage et al. 2011, 2014), modified for using the latest atomic data. Nonstatistical uncertainties were calculated from the uncertainty maps provided by XRT standard analysis software, `xrt_prep.pro`. The uncertainty maps from all images contributing to make the composite coronal image were processed into a composite uncertainty map. Then the uncertainty was collected from the corresponding area to the coronal image analysis as the square root of the sum of the uncertainty squared. These statistical and nonstatistical uncertainties together lead the uncertainties of Te and EM calculated by the XRT analysis software typically less than 0.1%. Note that, however, the absolute values of the obtained irradiance are more affected by a choice of filter pair, reliability of instrumental calibration, assumed atomic data on coronal plasma, or more inherently by the relevance of isothermal assumption of the corona. Although there is no easy way to include those uncertainties holistically, the resulting XRT irradiance contains not less than 50% of uncertainty with respect to its absolute value. Since our analysis here discusses relative values of signals and irradiances, the uncertainties given in Table 7 are more applicable.

XRT thin filters (e.g., Al-mesh and Al-poly) pass the EUV light near 20 nm (see Figure 9 of Narukage et al. 2011). The fractions are 0.03 for Al-mesh and 0.002 for Al-poly relative to the peak transmission of these filters both located at around 1 nm. Because of this EUV window, the signals observed with Al-mesh and Al-poly filters are dominated by strong EUV line emissions when the coronal temperature is closer to 1 MK, while it becomes almost negligible at the temperatures over 2 MK. It is important to note that these characteristics of XRT thin filters are included in their

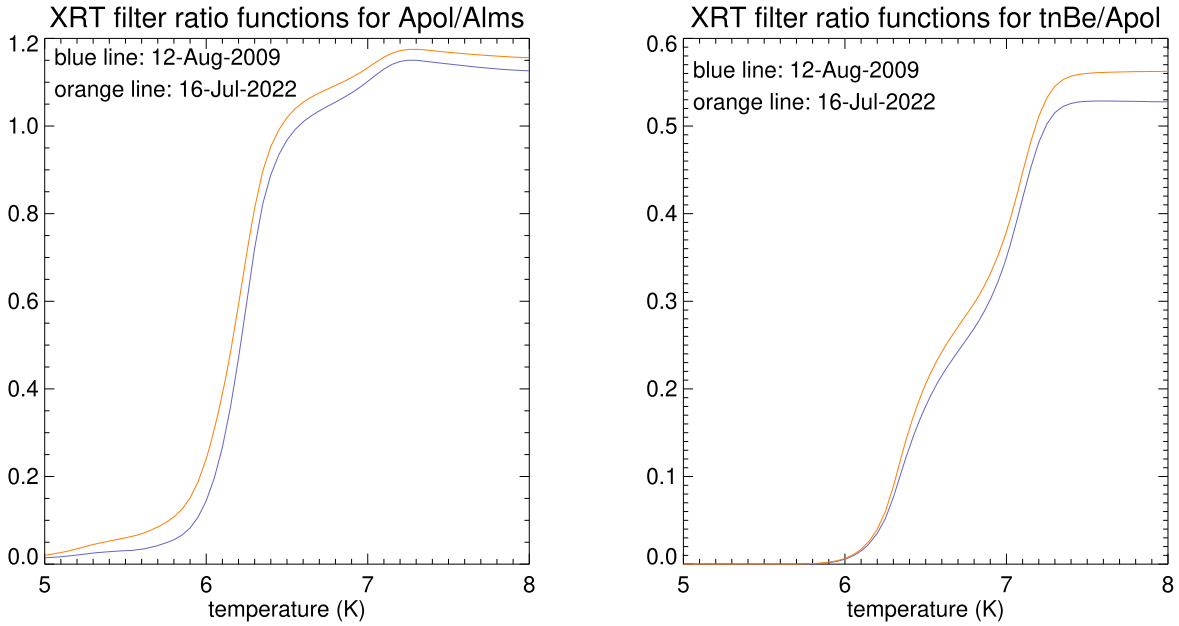

Figure 7. The ratios of the temperature response functions used in this work. The elemental abundance by Feldman (1992) was assumed. Left: the Al-poly/Al-mesh filter ratio. The blue (orange) line is used for the analysis of 2009 August 12 (2022 July 16) data. Right: the corresponding ratio curves from the thin-Be/Al-poly filter ratio.

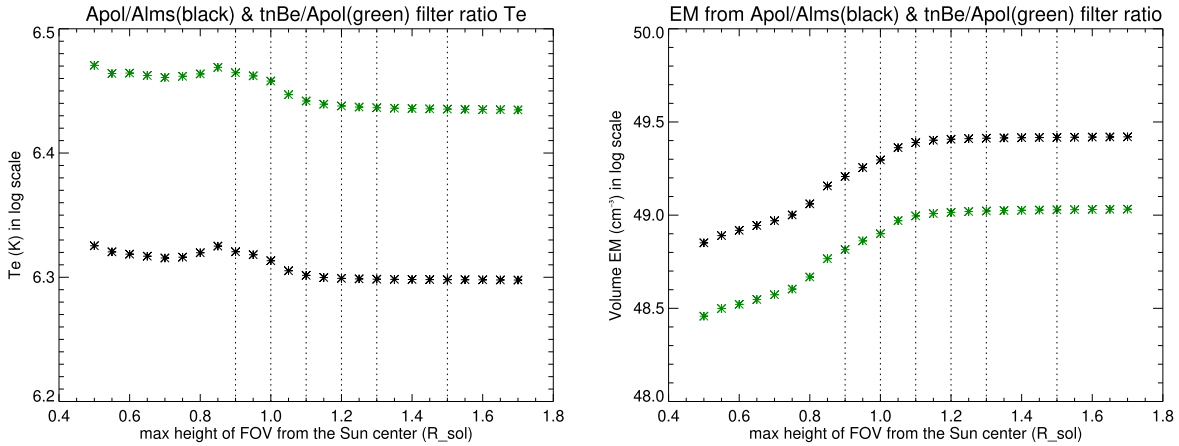

Figure 8. Filter ratio temperatures (left) and EMs (right) calculated for the active corona with FOVs of varying size. The symbols in black are derived from the Al-pol/Al-mesh filter ratio, while those in green are from thin-Be/Al-poly filter ratio.

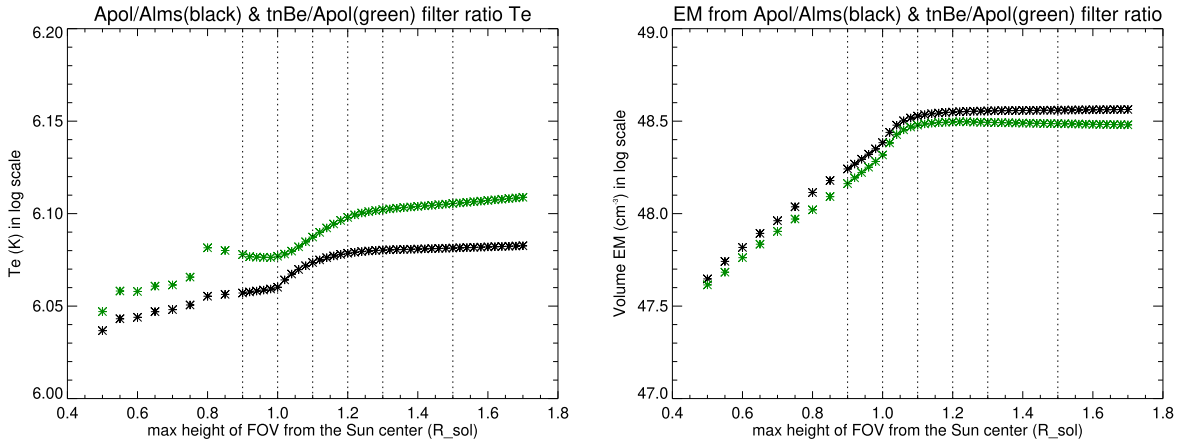

Figure 9. Same as Figure 8 but for the minimum corona calculated from the extended Te and EM plotted in Figure 6.

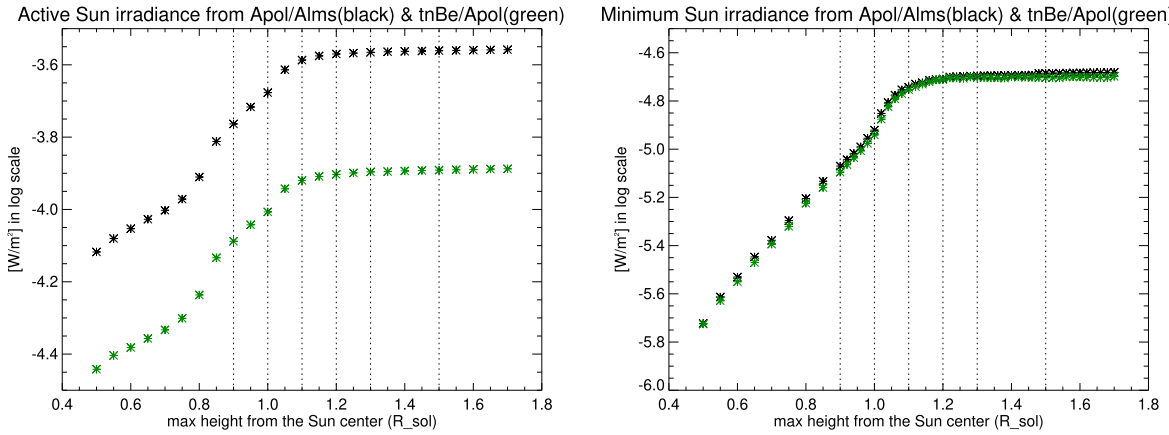

Figure 10. XRT irradiance (0.5–6 nm) obtained as a function of the size of FOV. Left : plot for active corona observed on 2022 July 16. Black symbols are data obtained from the Al-pol/Al-mesh filter ratio, while green symbols are from thin-Be/Al-poly filter ratio. The vertical dotted lines indicate the positions where the irradiance and its normalized value are listed in Table 5. Right : corresponding plot for the minimum corona observed on 2009 August 12.

Table 5
XRT Irradiance for the Active Corona Calculated from Al-poly/Al-mesh and Thin-Be/Al-poly Filter Ratios

FOV height ($R_\odot$)	Irrad. from Apol/Alms			Irrad. from tnBe/Apol		
	(10^{-4} W m^{-2})	Rel.	Exclusion frac. (%)	(10^{-4} W m^{-2})	Rel.	Exclusion frac. (%)
0.9	1.72	0.623	37.7	0.816	0.630	37.0
1.0	2.14	0.761	23.9	0.985	0.760	24.0
1.1	2.56	0.936	6.4	1.20	0.929	7.1
1.2	2.69	0.973	2.7	1.25	0.964	3.6
1.3	2.72	0.983	1.7	1.27	0.981	1.9
1.5	2.75	0.993	0.7	1.29	0.992	0.8
1.7	2.77	1.00	0.0	1.30	1.00	0.0

Note. Readings of Figure 10 for selected heights of FOVs were converted to a linear scale and listed in the unit of 10^{-4} W m^{-2}. The third and sixth columns are relative values to those at 1.7 $R_\odot$. The fourth and seventh columns are the exclusion fraction expressed in percentage. Note that these irradiance values are for a quarter area of the Sun. The full-Sun irradiance is estimated as roughly 4 times larger than the values listed here.

temperature response function and provide a valid (i.e., monotonically increasing) filter ratio to properly determine the temperature and EM over the range 0.1 to 10 MK (see Figure 7). Once the Te and EM are obtained, soft X-ray irradiance is calculated independently from the signals observed with XRT by calculating the isothermal coronal spectrum with the obtained value of Te and EM. Here the range of wavelength to calculate irradiance can be set arbitrarily. Therefore, calculating X-ray irradiance (0.5–6 nm) from the filter pair that includes EUV emissions is *not* logically incoherent.

While vignetting correction was performed in XRT's standard calibration software, `xrt_prep.pro`, the scattered light correction was not applied to the data used in the present analysis. The scattered light caused by imperfect reflection from the X-ray mirror is corrected by deconvolution of the modeled point-spread function (PSF). We initially applied this correction (with `xrt_deconvolve.pro`) and confirmed that it makes a difference of less than 0.1% in the total signal collected from each FOV. On the other hand, the correction significantly increases the roughness of the signal profiles as those illustrated in Figure 13. We therefore decided not to apply the PSF deconvolution in this analysis.

5. Discussions

Our data analysis demonstrated the possible fractions of Hinode/XRT irradiance excluded from the limited size of FOV, and their values differ between the active and the minimum corona. In this section, we will further investigate if these results are reproduced by other instruments of the same type, i.e., Yohkoh/SXT. We reprocessed the SXT full-Sun composite images used for Takeda et al. (2019) by applying the full-disk shaped FOV of three different radii, 0.9, 1.1, and 1.2 $R_\odot$. Pairs of thin-Al and AlMgMn (conventionally denoted as Al.1 and AlMg, respectively) filter signals within each FOV were used to calculate Te and EM, from which X-ray irradiance for the wavelength range 0.3–3 nm was obtained with Chianti atomic DB ver. 10.0 with the assumption of coronal elementary abundance by Feldman (1992).

5.1. Comparison of SXT and XRT Irradiances

Let $I_{1.2}$ and $I_{1.1}$ be SXT irradiances collected from the FOVs with the radius of 1.2 $R_\odot$ and 1.1 $R_\odot$, respectively. The mission-long variation of $I_{1.2}$ and $I_{1.1}$ in logarithmic scale (denoted as $\log I_{1.2}$ and $\log I_{1.1}$, respectively) smoothed over 14 days are presented in the top plot of Figure 11. We will estimate the average value of $I_{1.1}/I_{1.2}$ in the following way for three separate periods, I (1991 September–1995 December), II (1996 January–1997 June), and III (1997 July–2001 December), each roughly representing the declining, the minimum, and the rising phase of the solar cycle, respectively.

We first shift the $\log I_{1.1}$ curve upward by the constant value, a, as $\log I_{sft} = \log I_{1.1} + a$. We can find the value a^*, which minimizes the absolute value of the residual, i.e., $|\log I_{1.2} - \log I_{sft}|$, so that 10^{-a^*} indicates the best estimate of

Table 6
Same as Table 5 but for the Minimum Corona

FOV height ($R_\odot$)	Irrad. from Apol/Alms			Irrad. from tnBe/Apol		
	(10^{-5} W m^{-2})	Rel.	Exclusion frac. (%)	(10^{-5} W m^{-2})	Rel.	Exclusion frac. (%)
0.9	0.851	0.409	59.1	0.803	0.400	60.0
1.0	1.20	0.576	42.4	1.15	0.572	42.8
1.1	1.81	0.867	13.3	1.76	0.880	12.0
1.2	1.96	0.939	6.1	1.94	0.969	3.1
1.3	2.01	0.967	3.3	1.98	0.990	1.0
1.5	2.06	0.991	0.9	1.98	0.988	1.2
1.7	2.08	1.00	0.0	2.00	1.00	0.0

Note. Irradiances are in the unit of 10^{-5} W m^{-2}.

Table 7
Statistical and Nonstatistical Uncertainties Calculated by XRT Standard Software

FOV height ($R_\odot$)	Al-mesh		Al-poly		Thin-Be	
	Stat. (%)	Nonstat. (%)	Stat. (%)	Nonstat. (%)	Stat. (%)	Nonstat. (%)
Active corona images						
1.1	0.014	0.0114	0.016	0.0039	0.051	0.0080
1.3	0.013	0.0110	0.016	0.0038	0.050	0.0079
1.5	0.013	0.0109	0.015	0.0038	0.050	0.0079
1.7	0.013	0.0109	0.015	0.0038	0.050	0.0079
Minimum corona images						
1.1	0.022	0.0078	0.070	0.0105	0.855	0.1674
1.3	0.021	0.0083	0.067	0.0110	0.766	0.1634

the relative irradiance, $I_{1.1}/I_{1.2}$. We then define s as the rms of the residuals, $\log I_{1.2} - \log I^*_{sft}$, where $\log I^*_{sft}$ is the $\log I_{1.1}$ curve shifted by a^*, so that we can use the values $10^{-a^* \pm s}$ as a likely range of $I_{1.1}/I_{1.2}$ around the best estimated value. The calculated values of a^* and s, the best estimated values of $I_{1.1}/I_{1.2}$, and their likely ranges for different periods of solar cycle are listed in Table 8. The curve of $\log I^*_{sft}$ for each period is compared with that of $\log I_{1.2}$ in the bottom plot of Figure 11. Note that the numbers listed in Table 8 were calculated from unsmoothed daily averaged irradiance, while in Figure 11, smoothed data for 14 days are plotted for increasing visibility.

The averaged exclusion fraction of SXT irradiance by limiting the FOV to 1.1 $R_\odot$, i.e., the value $1 - (I_{1.1}/I_{1.2})$, is 10% for Period II, which is larger than the values for Periods I and III (both roughly 7%). This is consistent with the result from the XRT data: the corresponding results from XRT (converted to $I_{1.1}/I_{1.2}$ from Tables 6 and 7) are listed for comparison in the two right columns in Table 8. The values of $I_{1.1}/I_{1.2}$ for XRT minimum corona are similar to the best estimate of SXT for the Period II, while the exclusion fraction of XRT irradiance for the active corona (4%–5%) are generally smaller than the corresponding SXT results but within the average variation of SXT data.

5.2. Solar Cycle Variation of the Exclusion Fractions

In addition to the different exclusion fraction between the active and minimum corona, it is noticeable that the exclusion fraction of the rising phase (Period III) is slightly larger than the declining phase (Period I). Although this is not obvious from the numbers in Table 8, the plots of smoothed irradiances in Figure 11 clearly show that the values of a^* for Periods I and III are not interchangeable. This trend becomes more visible when the SXT irradiance from the FOV with the radius 0.9 $R_\odot$ ($I_{0.9}$, hereafter) is compared with that from 1.2 $R_\odot$ (i.e., $I_{1.2}$). Figure 12 and Table 9 demonstrate the plots and numbers for the comparison of $I_{0.9}$ and $I_{1.2}$, corresponding to those of Figure 11 and Table 8. The exclusion fraction averaged over Period III is 54%, which is larger than the value (50%) averaged over Period I. Although we have not been unable to eliminate the possibility that this difference is caused instrumentally (poor correction of stray light, etc.), a possible explanation of this result is that the coronal emission extends toward higher altitude in the rising phase than the declining phase of the solar cycle. Since sunspots started to appear at higher latitude in the rising phase, the corona above the high-latitude region becomes brighter. When it is observed from the Earth with limited FOV, the corona at higher altitude would look brighter, relative to other phases of solar cycle. This scenario needs to be confirmed by continued data acquisition with Hinode/XRT.

6. Summary

Using Hinode/XRT images of solar corona, we investigated how instruments' limited FOV affects the observed soft X-ray irradiance. XRT images obtained with three X-ray analysis filters (Al-mesh, Al-poly, and thin-Be) at different solar activity levels were analyzed and compared: the NE quadrant images of the Sun observed up to 1.7 $R_\odot$ on 2022 July 16 were used for studying the active Sun. On the other hand, the full-Sun images obtained on 2009 August 12 were analyzed as the case of minimum corona. The masking image of varying size and the shape tailored for each case were applied to measure the total signal from a quarter area of the Sun with different sizes of FOV. For the minimum corona, the signals collected from the increasing size of FOV can be measured up to 1.3 $R_\odot$, but the curve of variation was extended to 1.7 $R_\odot$ by assuming the

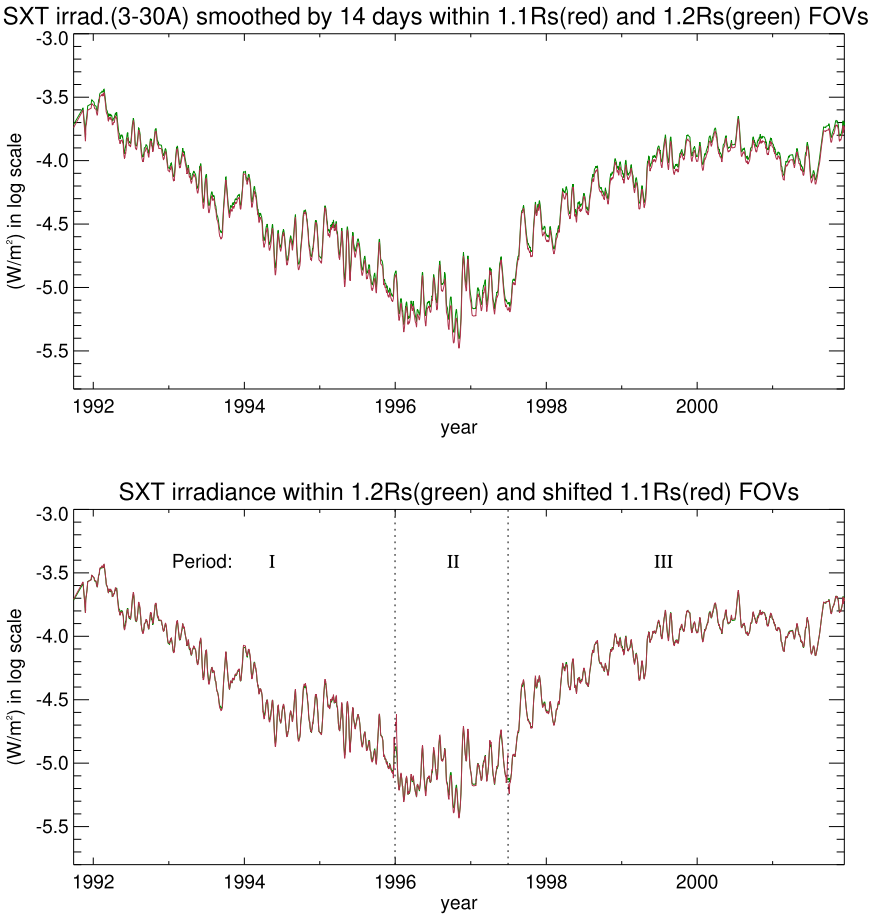

Figure 11. Top: mission-long Yohkoh/SXT irradiance (0.3–3 nm) obtained from two different FOV sizes. Green and red lines are from the FOV radii, 1.2 $R_{\odot}$ and 1.1 $R_{\odot}$, respectively. Bottom : SXT irradiance from the FOV radii 1.2 $R_{\odot}$ (green) and the curve of irradiance with 1.1 $R_{\odot}$ FOV shifted by the amount a^* in the Table 8 (red). See the text in Section 5.1 for details.

Table 8
Comparison of Relative Yohkoh/SXT Irradiance, $I_{1.1}/I_{1.2}$ with the XRT Relative Irradiance for the Corresponding Period of the Solar Cycle

Period	SXT Irrad. $I_{1.1}/I_{1.2}$					XRT Irrad. $I_{1.1}/I_{1.2}$	
	a^*	s	10^{-a^*}	10^{-a^*-s}	10^{-a^*+s}	Apol/Alms	tnBe/Apol
I	0.0320	0.0189	0.929	0.889	0.970	…	…
II	0.0460	0.0257	0.899	0.848	0.954	0.923	0.907
III	0.0335	0.0161	0.926	0.892	0.961	0.952	0.960

Note. Relative Yohkoh/SXT irradiance (fourth column) is compared with the XRT relative irradiance for the corresponding period of the solar cycle (seventh and eighth columns). See the text in Section 5.1 for details.

Table 9
Comparison of Relative SXT Irradiance, $I_{0.9}/I_{1.2}$ with the XRT Relative Irradiance for the Corresponding Period of the Solar Cycle

Period	SXT Irrad. $I_{0.9}/I_{1.2}$					XRT Irrad. $I_{0.9}/I_{1.2}$	
	a^*	s	10^{-a^*}	10^{-a^*-s}	10^{-a^*+s}	Apol/Alms	tnBe/Apol
I	0.300	0.167	0.501	0.342	0.735	…	…
II	0.354	0.200	0.443	0.279	0.701	0.434	0.414
III	0.336	0.161	0.461	0.318	0.668	0.639	0.653

Note. See note for Table 8.

radial decreasing rate of the azimuthally averaged signals similar to the case of active corona. The ratio of a pair of filter signals was used to derive filter-ratio temperatures (Te) and EMs averaged over the FOV. The XRT irradiance was obtained as the energy spectrum of the isothermal corona (having Te and EM) integrated over 0.5–6 nm.

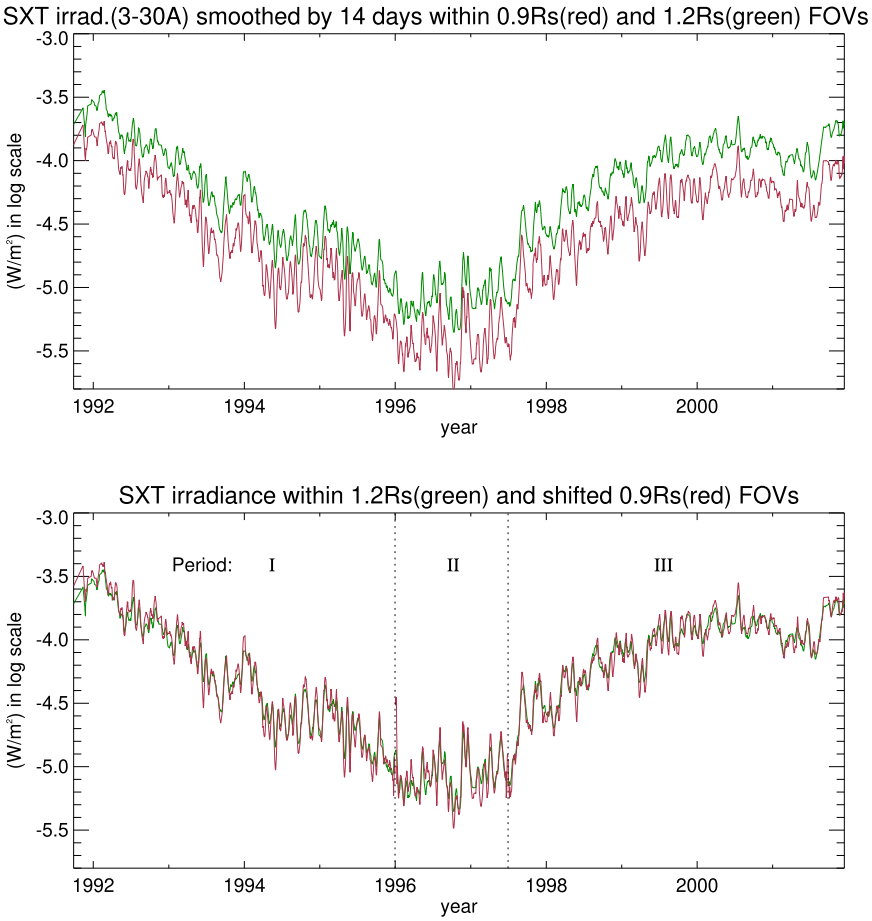

Figure 12. Top: mission-long Yohkoh/SXT irradiance (0.3-3 nm) obtained from two different FOV sizes. Green and red lines are from the FOV radii, 1.2 $R_{\odot}$ and 0.9 $R_{\odot}$, respectively. Bottom : SXT irradiance from the FOV radii 1.2 $R_{\odot}$ (green) and the curve of irradiance with 0.9 $R_{\odot}$ FOV shifted by the amount a^{*} in the Table 9 (red). See the text in Section 5.1 for details.

The goal of this study is to provide a guide to quantitative correction of X-ray irradiances obtained from different sizes of FOV, rather than increasing the precision of the measurements of the X-ray irradiance on a particular day. An example of the results is that the irradiance obtained within 1.1 $R_{\odot}$, which is the FOV of XRT irradiance study, excludes $\sim$3.5%/$\sim$7% of irradiance relative to the value within 1.2/1.7 $R_{\odot}$, respectively, for the active corona observed in 2022 July, while on the contrary, the excluded fraction increases to $\sim$7%/$\sim$13% respectively for the minimum corona observed in 2009 August. In order to observe the XRT irradiance with less than 1% exclusion fraction for both active and minimum corona, it is desirable to observe up to the height of 1.5 $R_{\odot}$.

To confirm the irradiance exclusion fractions depending on the solar activity level, we reprocessed Yohkoh/SXT full-Sun images used for SXT irradiance study with 1.2 $R_{\odot}$ FOV (Takeda et al. 2019) to obtain the irradiance up to 1.1 $R_{\odot}$ and 0.9 $R_{\odot}$. We separated the mission period into three phases of the solar cycle, the declining phase (1991 September–1995 December), minimum phase (1996 January–1997 June) and rising phase (1997 July–2001 December) and compared the average exclusion fraction relative to that for 1.2 $R_{\odot}$ for different phases of solar cycle. It was confirmed for both irradiances within 1.1 $R_{\odot}$ and 0.9 $R_{\odot}$ that the exclusion fractions of minimum phase were the largest among the three. In addition, it was found that the exclusion fraction of the rising phase is slightly larger than that of declining phase. Further investigation is to be performed, but a possible interpretation is that the larger expansion of hotter plasma is over the higher-latitude region in the rising phase than the declining phase.

Acknowledgments

This work was supported partly by a grant from NSF's Research Experiences for Undergraduates (REU) program held at MSU in 2022. Hinode is a Japanese mission developed and launched by ISAS/JAXA, with NAOJ as domestic partner and NASA and STFC (UK) as international partners. It is operated by these agencies in cooperation with ESA and NSC (Norway). The Yohkoh mission was developed and launched by ISAS/JAXA, Japan, with NASA and SERC/PPARC (UK) as international partners. This work made use of the Yohkoh Legacy data Archive at Montana State University, which was supported by NASA. CHIANTI is a collaborative project involving George Mason University, the University of Michigan (USA), University of Cambridge (UK) and NASA Goddard Space Flight Center (USA).

Facilities: Hinode (XRT), Yohkoh (SXT).

Software: SolarSoft (Freeland & Handy 1998), CHIANTI ver.10 (Dere et al. 1997; Del Zanna et al. 2021).

Appendix
Derivation of Radial Intensity Variation

The purpose of this appendix is to provide a reasonable way to extend the curve of integrated signals of the minimum corona from the observed 1.3 $R_\odot$ (Figure 5) to nearly 1.7 $R_\odot$, the same height as the active corona data (Figure 6). We will assume the decreasing rate of the signals in radial direction being similar to the active corona, and thus, we first process the image of the active corona to derive the averaged radial variation of XRT signals.

A.1. The Active Corona of 2022 July 16

We consider the XRT signals as a function of r, the radial distance from Sun center and θ, the position angle counterclockwise from the north pole, as $S(r, \theta)$. The total signal included in the quarter-disk-shaped FOV with the height of r_0 is written as

$$A(r_0) = \int_0^{r_0} dr \int_0^{\pi/2} rd\theta\ S(r, \theta). \tag{A1}$$

The number of pixels included in the same area is

$$N(r_0) = \int_0^{r_0} dr \int_0^{\pi/2} rd\theta\ n_0(r, \theta), \tag{A2}$$

where n_0 is the number of pixels per unit area. We define the radial variation of the signals averaged over the position angle with the following equation:

$$S_{\rm rad}(r + dr/2) = [A(r + dr) - A(r)]/[N(r + dr) - N(r)]. \tag{A3}$$

$S_{\rm rad}$ was calculated for the active corona observed on 2022 July 16 with r increasing from 0.9 to 1.7 $R_\odot$ with $dr = 0.02\ R_\odot$ and presented in the Figure 13, left plot. We then defined the averaged radial decreasing rate as

$$D_{\rm rad}(r) = S_{\rm rad}(r + dr/2) - S_{\rm rad}(r - dr/2). \tag{A4}$$

We calculated $D_{\rm rad}$ for r 0.89 to 1.69 $R_\odot$ with $dr = 0.02\ R_\odot$ and presented in the right plot of Figure 13.

A.2. The Minimum Corona of 2009 August 12

The same series of procedures was applied to the images of the minimum corona. The left plot of Figure 14 shows the calculated $S_{\rm rad}$ together with two actual profiles along the lines displayed in the Al-mesh image of Figure 2. The right plot of Figure 14 is the variation $D_{\rm rad}$, but the data points up to 1.3 $R_\odot$ are those from the observed data. Those beyond 1.3 $R_\odot$ were

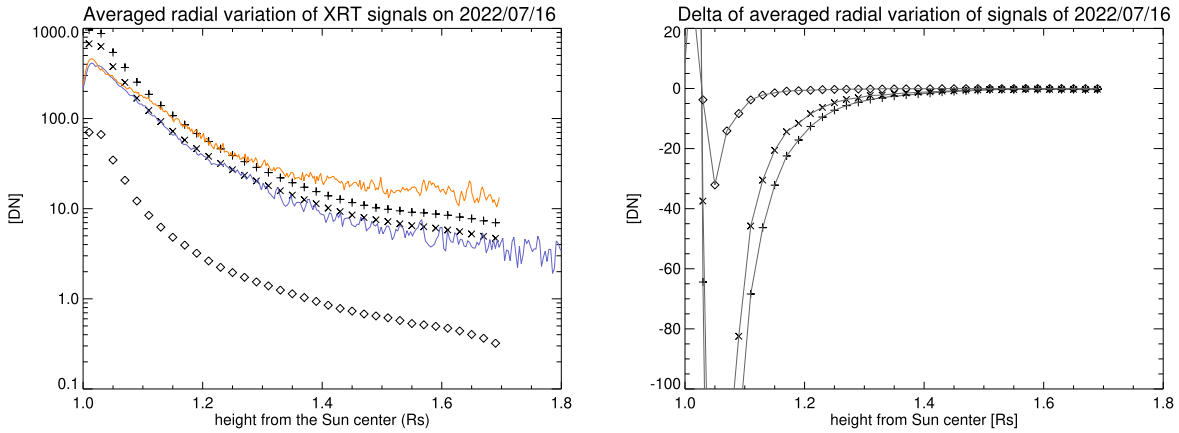

Figure 13. Left: averaged radial variation of XRT signals for the active corona observed on 2022 July 16. Actual Al-mesh signal profiles at the locations shown in solid lines in the Al-mesh image (leftmost) of Figure 1 were also plotted for comparison. The radial curves are all monotonically decreasing and demonstrate the ghost patterns indicated in Figure 1 having a negligible effect. Right: averaged radial decreasing rate of the XRT signals obtained from the left plot.

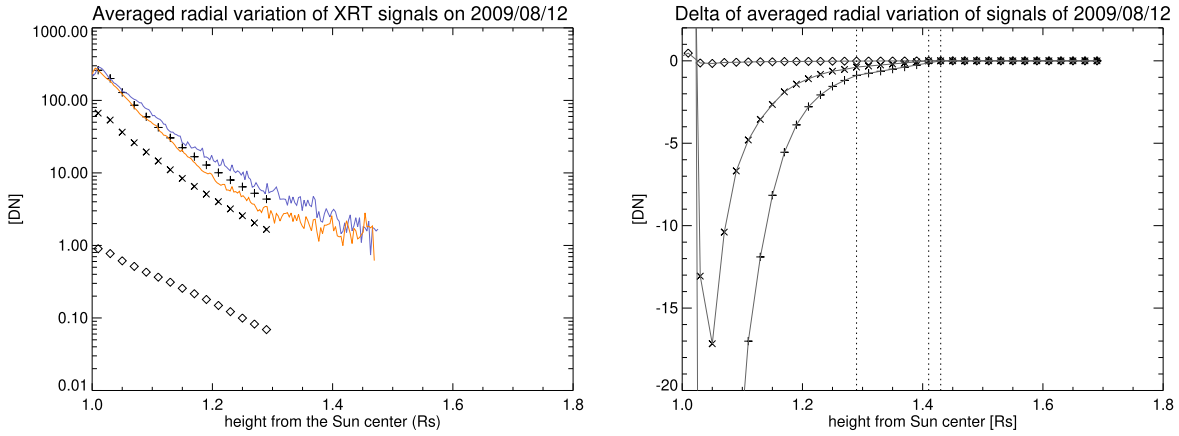

Figure 14. Left: averaged radial variation of XRT signals for the minimum corona observed on 2009 August 12. Actual Al-mesh signal profiles at the locations shown in solid lines in the Al-mesh image (leftmost) of Figure 2 were also plotted for comparison. Blue/orange lines are those of northwest/southeast directions, respectively. Right: averaged radial decreasing rate of the XRT signals obtained from the left plot.

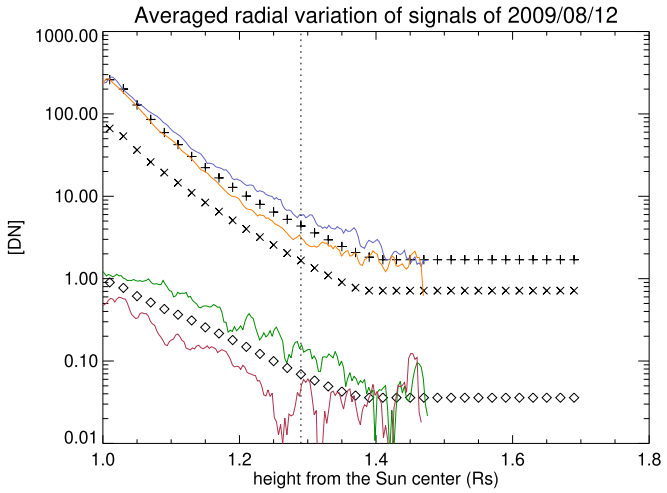

Figure 15. Averaged radial variation of XRT signals for the minimum corona extended using the assumed decreasing rate in Figure 14, right plot. Again for comparison, the actual profiles from Al-mesh and thin-Be images are overplotted. Green/red lines show thin-Be profiles of NW/SE directions, respectively.

added so as to approach smoothly to zero: for the Al-mesh filter, data points were assumed to linearly approach zero at the height of 1.43 $R_{\odot}$, while those of Al-poly and thin-Be filters were assumed similarly to be zero at 1.41 $R_{\odot}$.

The $S_{\rm rad}$ curves recovered from the observed and extended $D_{\rm rad}$ are presented in Figure 15. It turns out that the extended $S_{\rm rad}$ curves represent well the actual profiles roughly up to 1.45 $R_{\odot}$. Using the data points in Figure 15, the extended curves of total signals in the FOVs were calculated and plotted in Figure 6.

ORCID iDs

Aki Takeda https://orcid.org/0009-0001-4785-2265

References

Chamberlin, P. C., Woods, T. N., Eparvier, F. G., & Jones, A. R. 2009, Proc. SPIE, 7438, 743802
Dere, K. P., Landi, E., Mason, H. E., Fossi, B. C. M., & Young, P. R. 1997, A&AS, 125, 149
Del Zanna, G., Dere, K. P., Young, P. R., & Landi, E. 2021, ApJ, 909, 38
Didkovsky, L., Judge, D., Wieman, S., Woods, T., & Jones, A. 2012, SoPh, 275, 205
Feldman, U. 1992, PhyS, 46, 202
Freeland, S. L., & Handy, B. N. 1998, SoPh, 182, 497
Garcia, H. A. 1994, SoPh, 154, 275
Golub, L., DeLuca, E., Austin, G., et al. 2007, SoPh, 243, 63
Kobelski, A. R., Saar, S. H., Weber, M. A., McKenzie, D. E., & Reeves, K. K. 2014, SoPh, 289, 2781
Lin, C. Y., Bailey, S. M., Jones, A., et al. 2016, JGRA, 121, 3648
Mithun, N. P. S., Vadawale, S. V., Sarkar, A., et al. 2020, SoPh, 295, 139
Moore, C. S., Caspi, A., Woods, T. N., et al. 2018, SoPh, 293, 21
Narukage, N., Sakao, T., Kano, R., et al. 2011, SoPh, 269, 169
Narukage, N., Sakao, T., Kano, R., et al. 2014, SoPh, 289, 1029
Takeda, A., Acton, L., & Albanese, N. 2019, ApJ, 887, 225
Takeda, A., Yoshimura, K., & Saar, S. H. 2016, SoPh, 291, 317
Tsuneta, S., Acton, L., Bruner, M., et al. 1991, SoPh, 136, 37
White, S. M., Thomas, R. J., & Schwartz, R. A. 2005, SoPh, 227, 231
Woods, T. N., Eparvier, F. G., Bailey, S. M., et al. 2005, JGRA, 110, A01312
Woods, T. N., Eparvier, F. G., Hock, R., et al. 2012, SoPh, 275, 115